

---

## Characterization of gasbearing sediments in coastal environment using geophysical and geotechnical data

Dusart Judith <sup>1,2,\*</sup>, Tarits Pascal <sup>1,2</sup>, Fabre Maud <sup>1</sup>, Marsset Bruno <sup>3</sup>, Jouet Gwenael <sup>3</sup>, Ehrhold Axel <sup>3</sup>, Riboulot Vincent <sup>3</sup>, Baltzer Agnes <sup>4</sup>

<sup>1</sup> European Institute for Marine Studies (IUEM) ,Plouzané , France

<sup>2</sup> Mappem Geophysics SAS Saint-Renan , France

<sup>3</sup> Ifremer, Plouzané , France

<sup>4</sup> University of Nantes, Lab Geolittomer Nantes 3, France

\* Corresponding author : Judith Dusart, email address : [judith.dusart@mappem-geophysics.com](mailto:judith.dusart@mappem-geophysics.com)

---

### Abstract :

Seismic investigation in marine gas-bearing sediments fails to get information below the acoustic mask created by free gas. To circumvent this problem, we combined collocated multichannel ultra-high resolution seismic imaging, marine electrical resistivity tomography (MERT) and core sampling to study the physical properties of gas-bearing sediments in the Bay of Concarneau (France). We obtained sections of compression (P-) wave velocity values where free gas was identified in seismic data. We tested a joint processing workflow combining the 1D inversion of the MERT data with the 2D P-wave velocity through a structural coupling between resistivity and velocity. We obtained a series of 2D resistivity models fitting the data whilst in agreement with. The resulting models showed the continuity of the geological units below the acoustic gas fronts which is associated with paleo-valley sediment infilling. We were able to demonstrate relationships between resistivity and velocity differing from superficial to deeper sediments. We established these relationships at the geophysical scale then compared the results to data from core sampling (porosity). We inferred the porosity distribution from the MERT data. At the core locations, we observed a good agreement between this geophysical scale porosity and the core data both within and outside the gas-bearing sediments. This agreement demonstrated that resistivity could be used as a proxy for porosity where no was available below gas caps. In these regions, the observed low resistivity showed a high porosity (60-70%) down to about 10–20 m in depth in contrast with the surrounding medium with porosity less than 55%. These results support the hypothesis that failures inside the paleo-valley sediment could control the gas migration

**Keywords :** Shallow gas, Electrical Resistivity Tomography, modelling, seismic, porosity

## INTRODUCTION

Gas-bearing marine sediments are very common and widely found across the world (Fleischer *et al.* 2001). They have been largely studied as they are known to cause major accidents such as well blow-outs (Thi Van Ngo and Ferguson 2020), possible sinking of ships (Deming 2004) or drilling rigs (Prince 1990). The predominant biogenic gas in marine sediments is methane, a well-known and powerful greenhouse gas (Hovland and Judd 1992), much studied in the context of climate change. Gas-bearing marine sediments have practical (related to imaging and engineering issues), environmental and safety significance (Fleischer *et al.* 2001). Thus, the identification and avoidance of shallow gas is a principal objective during site survey procedures (Thi Van Ngo and Ferguson 2020).

Free gas is widespread and can be found worldwide in sediments of shallow marine environments (Fleischer *et al.* 2001). The ideal environment for the accumulation of gas is a rapidly accumulating,

This article is protected by copyright. All rights reserved.

fine-grained muddy sediment rich in organic matter. Such areas are mainly located in coastal shallow-water environments (Fleischer *et al.* 2001). The Bay of Concarneau (France) is a good example, showing numerous shallow gas evidence in the near-surface sediment layers (Baltzer *et al.* 2014).

Shallow gas can have either a thermogenic or a biogenic origin. Biogenic methane is produced by the degradation of organic matter caused by bacterial activity at low temperatures near the seafloor, whereas thermogenic methane is produced deeper by chemical reactions within the sediment at higher temperatures (Rice and Claypool 1981). When pore water methane concentrations exceed saturation levels, free methane forms in the sediment (Martens and Klump 1980).

Shallow gas is challenging for classical imaging techniques. On seismic data, free gas can be easily identified as gas bubbles have a strong acoustic signature. Indeed, within the stratigraphic column, free gas has a masking effect on seismic data because of their scattering action on the acoustic signal, thus limiting the depth of investigation. Even in small quantities, and especially for shallow gas, bubbles can cause strong compressional wave attenuation, reducing the compression (P-) wave velocity (Anderson and Hampton 1980; Wilkens and Richardson 1998; Gardner 2000). The P-wave velocity is particularly low when free gas is present (down to  $\sim 700$  m/s), and usually ranges between 1350 and 1500 m/s (Lee *et al.* 2009; Kim *et al.* 2014; Garcia *et al.* 2014). Based on the reduction of P-wave velocity in gassy sediments, *in situ* amounts of free gas may be estimated using the velocity field obtained from seismic data. These approaches show that gas content as low as 1–2% reduces the velocity by several hundreds of m/s (Toth *et al.* 2014).

Geotechnical studies showed that gas-bearing sediments increase seabed compressibility and reduce its undrained shear strength (Sills and Wheeler 1992; Kim *et al.* 2014). They also reduce the intrinsic permeability and possibly have a high excess pore pressure (Sultan *et al.* 2007).

As shallow gas is both limiting seismic imaging and altering physical properties of the sediment, the aim of this study is to circumvent the former and better characterise the latter by combining several complementary study methods. Aside traditional methods (seismic imaging, core sampling), our study adds another imaging method: marine electrical resistivity tomography (MERT). Unlike seismic methods, resistivity data do not suffer from scattering effects of free gas. The electrical resistivity can be obtained with MERT (*e.g.*, Tarits *et al.* 2012) or marine controlled source electromagnetic methodology (*e.g.*, Constable, Kannberg and Weitemeyer 2016). For high gas saturation level, gas-bearing sediments proved to appear slightly more electrically resistive than similar gas-free sediment, as free gas does not conduct the electrical current (Goswami *et al.* 2016).

Our study combines ultra-high resolution (UHR) multichannel seismic imaging, core sampling (analysed with a multi-sensor core logging, MSCL, bench) and MERT to reach the following goals:

- 1) to investigate the nature, geometry and physical properties of the geology in a shallow-gas environment,
- 2) to circumvent limiting effects of gas on seismic imaging and get geological information below the gas caps,

3) to identify the specific properties of gas-bearing sediments compared to the surrounding geological units,

4) to deduce information on gas content in the study area.

The joint use of UHR multichannel seismic imaging and MERT is first carried out as a close comparison between the results, which were combined with the MSCL results to investigate the properties of the sediment and especially the relationships between P-wave velocity, resistivity, and porosity. These relationships describe the physical and mechanical properties of the gas-bearing marine sediment. Then, a joint processing workflow is developed between seismic and resistivity data through a constrained inversion process. This new approach has two main objectives: improving the resistivity models by adding structural information into the inversion process; and circumventing the masking effect of gas bubbles on seismic data. Finally, from the joint analysis of the data, the gas content is qualitatively characterized, and a porosity model is proposed from the MERT data using the Archie's law.

#### GEOLOGICAL SETTING

The study area is located off the French coast, in the Bay of Concarneau (southern coast of Brittany) (Figure 1). The area approximately covers 200 km<sup>2</sup> (5-6 km wide and ~8.8 km long), between the Trévignon headlands and the Glénan Islands and above the 40 m isobaths below Low Astronomic Tide (LAT). The slope is oriented south-eastwards in the direction of the Tertiary Kerforne fault system (Delanoë and Pinot 1977). On the eastern boundary, the coastal topography features a terrace of shoals, whose foot is bounded by the -20 m isobaths LAT (Delanoë and Pinot 1977; Raimbault *et al.* 2018). The geophysical and geotechnical surveys were obtained for water depths ~25-30 m LAT.

The geology comprises middle Eocene sandstone and sandy limestone formations (units U1 and U2 in Raimbault *et al.* 2018; Figure 2a), overlapping onto the crystalline basement. Several paleovalleys incise the substratum. Two palaeovalley systems, oriented N160 (Kerforne system), have been excavated from the end of the Eocene to the beginning of the Oligocene (unit U2) (Pinot 1974; Menier *et al.* 2006). The large drainage system is infilled by coarse fluvial continental (unit U3) and estuarine Pleistocene deposits (unit U4). A Holocene sedimentary layer 3 to 5 m thick composed of mud and sand covers the entire area (Jouet *et al.* 2019, Menier 2003; unit U5).

The Bay of Concarneau is characterized by a large and dense field of pockmarks (Ehrhold, Hamon and Guillaumont 2006; Baltzer *et al.* 2014) whose diameters are up to 30 m, forming 2 m deep depressions, formed by fluid escape from gas-saturated sediment. This field is present in water depths <30 m and covers an area of 36 km<sup>2</sup> (Baltzer *et al.* 2017). The pockmarks density unusually reaches ~6000 per km<sup>2</sup> in places (Baltzer *et al.* 2017; Figure 1). The gas is concentrated within the geological unit U5 (Figure 2a) which corresponds to tidal flat deposits and coarse lag deposits within tidal channels. The thickness of unit U5 generally increases in the paleo-river valleys.

Sidescan sonar images revealed that numerous pockmarks (morphological features associated to fluid escapes; Judd and Hovland 2009) were infilled with muddy deposits (low backscattering inside

of pockmarks), whereas in the middle and southernmost sectors, most of the pockmarks lacked infilling (Ehrhold *et al.* 2006). The rapid sedimentary infilling of the paleovalleys during the Holocene transgression could explain the formation of biogenic methane wherever the thickness of the sediment cover (unit U3) is sufficient (Baltzer *et al.* 2014). Even though pockmarks often correspond to a thermogenic origin of methane, this was supposed highly improbable in the Bay of Concarneau as the basement mainly consists in crystalline rocks with no potential deep gas reservoirs (Baltzer *et al.* 2014). Some gas plumes were also observed in the Bay, suggesting a current activity of the pockmark field (Baltzer *et al.* 2014).

Baltzer *et al.* (2014) have conducted gas and pore water analyses on cores taken in the Bay of Concarneau. Pore-water analyses revealed that methane concentrations were close to zero in the upper 6 cm (below the seafloor) of a core sampled in a pockmark, and then increased to peak at 383 and 415  $\mu\text{L/L}$  at 22 and 30 cm in the silty sediment. Outside of pockmarks, the methane levels were much lower ( $<5 \mu\text{L/L}$ ; Baltzer *et al.* 2014). Deeper, the quantity of free gas in the sediment is difficult to measure because methane degasses when the sediment is brought to ambient pressure during core recovery (Toth *et al.* 2014). In our study area, no measurement of methane concentration is available in the literature below 4 m below seafloor (BSF).

## DATA AND METHODS

### Core data

The site of Concarneau was studied using core sampling in 2018 during the SYPOCO campaign (Ehrhold and Riboulot 2018). 41 Kullenberg cores of  $\sim 4$  m long were extracted and analysed using a MSCL bench. This device is equipped with several sensors, measuring the gamma density, the P-wave velocity, gamma attenuation, and magnetic sensibility along the core. From the gamma density, the porosity was evaluated using  $2.66 \text{ g/cm}^3$  as mineral grain density (Das and Sivakugan 2016) and  $1.024 \text{ g/cm}^3$  as fluid density. Grain size analysis was available for three cores extracted on the study area, showing an average of 80% of fine particles (mud, silt, clay) and 20% of sand for the superficial sediment layer. These cores were not located on the geophysical lines.

### UHR multichannel seismic reflection

#### Seismic acquisition

Geotechnical data were completed with UHR multichannel seismic imaging during the two cruises ESS FLUTE in 2016 (Marsset 2016) and SYPOCO in 2018. Seismic data were acquired with two different multichannel streamers; one with 48 channels 3.125 m apart and one with 48 channels divided into 24 channels 1 m apart and 24 channels 2 m apart. Such streamers are optimized for shallow areas with bathymetry not exceeding 75 m.

The acoustic source was a Sparker whose acoustic signal is created by electrical discharges of a capacitor bank in an immersed multi-tip electrode. The Sparker was operated with a 160 J energy

and a 100 tips electrode, a trade-off between energy and frequency content to minimize the signature duration and optimize vertical resolution. The frequency content lied between 200 and 1650 Hz. The shooting rate was set to 350 ms and the acquisition speed to 4 knots providing the necessary fold for P-wave velocity determination.

The depth of investigation (maximum penetration) was  $\sim 60$  m BSF, when not reduced by the blanking effect of free gas. The study focused on the lines presented in Figure 1.

### Seismic processing

Seismic data went through a standard processing workflow using the in-house software SolidQC from Ifremer, and the commercial software proMAX. After processing of the acquisition geometry and the navigation data, the source signal was analysed and processed using a deconvolution step (Jovanovich, Summer and Akins-Easterlin 1983). This deconvolution reduced ghost signals and allowed recovering a pulse signal which improved the vertical resolution on the data. The swell was corrected. When existing, the refracted waves were muted. The processed seismic traces were then sorted on a grid with a 1 m bin.

Semblance panels were calculated through a Normal Move Out (NMO) algorithm in order to determine  $V_p$ . The velocity was calculated every 100 m along all studied lines (Figure 1) excepting ESS\_FLUTE\_24 for which the velocity was calculated every 25 m. A summation (stack) was then performed followed by Kirchhoff migrations both in time and in depth. The refined velocity analysis allowed removing the multiples except for areas where free gas created an acoustic mask.

For line ESS\_FLUTE\_24, the P-wave velocity model was obtained after a processing workflow oriented to highlight lateral structures, homogeneous layers, and geological interpretation. The P-wave velocity was laterally smoothed following consistent interfaces chosen based on geological consistency criteria. A 2D convolution filter (2 ms two way traveltime, TWT, vertically and 60 m laterally) was applied layer by layer to highlight the geological structures.

A tide correction was applied to the final section. At the end of the processing workflow, the vertical resolution was evaluated to 1 m and the horizontal to 5 m.

### **Marine Electrical Resistivity Tomography (MERT)**

#### MERT acquisition

During the cruise SYPOCO in 2018, we carried out a MERT survey along some of the seismic lines (Figure 1) with the MAPPEM acquisition system (Tarits *et al.* 2012). The system was configured with a dipole-dipole layout. We acquired 24 km of MERT sections along eight lines.

The system comprised a main fish, a smaller one forming an injection dipole transmitting a DC current of 25 A at low voltage, and a streamer with 20 electric potential electrodes. The system attitude was obtained from altitude, depth, and bidirectional tilt sensors. The transmitter dipole was

10.9 m long. The 20 receivers were 4 m apart and located 11 m behind the transmitter. The system had a total length of 107.5 m and was towed at an altitude of about 3 m above the sea floor at 3-4 knots.

The depth of investigation (DOI) and the minimum vertical resolution depend on the size of the system and were approximatively estimated as 20-25 m and  $\sim 5\%$  of the depth, respectively. Each sounding consisted of 19 electric potentials repeated with a spatial sampling depending on the ship velocity. During the survey, the current injection rate was 0.5 s, thus 0.8-1.0 m at 3-4 knots. The uncertainty of each measurement was estimated from the standard deviation of the potential difference measured when current was not injected (ambient noise). The uncertainty increased with the distance between the injection dipole and the reception dipole and ranged between  $\sim 0.03$  and  $\sim 8.3\%$ .

#### MERT processing

The data processing was carried out using both built-in software and processing codes adapted to the MAPPEM system. The processing workflow consisted in attitude data cleaning to remove abnormal jumps and artefacts. Then, the location of each measurement was obtained from the combination of GPS data on the ship and the layback continuously monitored (uncertainty of  $\sim 5$  m). Taking stock of the simultaneous acquisition of the 19 potential differences and using the geometry of the system, we scaled the data into apparent resistivity (electrical resistivity of an equivalent homogeneous space).

For a given profile, the data set consisted of the apparent resistivity values and its standard deviation as a function of the offset (distance between receiver and transmitter) and position along the profile. The relationship between apparent resistivity and true resistivity is non-linear and data inversion must be performed to recover the true resistivity as a function of depth and position. In our study, this operation was carried out using two methods: a 2D commercial software and a 1D built-in algorithm using the prior structural information given by seismic data (constrained inversion).

#### 2D inversion with Res2DInv

Electric sounding data inversion is well known. Various algorithms exist in 1D, 2D and 3D (Loke 2004; Sharma and Verma 2015). In this study, we used a modified version of the commercial software RES2DINV (Loke 2016) adapted to our data set. This version of the software enables 2D inversion of the whole set of data and a variable resistivity of the water layer. The resulting models provide reasonably reliable values of the resistivity ground values BSF so we can use them to compare to the geotechnical data.

The layering was defined according to the maximum depth of investigation, the minimum resolution, and the results of the inversion tests. The thickness of the first layer was 0.5 m, the increasing factor with depth was 1.1 and the bottom depth was set to twice the maximum DOI, which corresponds to

about 45 m below the acquisition system. The model had a total number of 32 layers. Above the seafloor, the water layer could be split to include resistivity values measured with a Conductivity Temperature Depth (CTD) probe at the beginning and at the end of the survey.

The inversion was tested for several norms and regularization terms. Eventually we used the L2-norm and a flatness filter directly applied on the model. We found that the careful estimate of the data standard deviations improved the inversion results in reducing the impact of possible artefacts and improving the accuracy of the final resistivity models.

The survey lines were composed of 1303 to 6874 soundings, thus, too long to be inverted at once with Res2DInv. Each line was split into sub-sections of 1000 soundings maximum that were inverted separately and then stitched together. All inverted sections overlapped by 420 soundings to create seamless profiles. The final root mean square (RMS) error was less than 1.5% for all sections.

### 1D constrained inversion

We also used a second inversion method by combining resistivity and velocity in a constrained inversion to infer common geometrical features between the two parameters and identify the geological units and their boundaries in the seismic mask region. Indeed, Res2DInv is not an open source and cannot be modified to include new features such as joint inversions with data of different nature, *i.e.*, seismic velocity in this study. Before undertaking the lengthy process developing our own constrained inversion 2D code, we tested the constrained inversion approach with a 1D inversion solution. The 1D approach has the advantage of being fast to invert the long survey lines in one time.

The 1D approximation is reasonable because the seawater-saturated sediments and rocks have a very low resistivity, changing by small values along a section (Figure 2c and Figure 3c). This is in contrast with land resistivity survey where apparent resistivity may change per orders of magnitude along a section. The algorithm was developed specifically for this application and is based on a non-linear steepest gradient method.

The inversion algorithm proceeds by minimizing a cost-function formed by different weighted terms. All 1D resistivity profiles were smoothed vertically using a regularization term  $R$  based on a variance calculation. The 1D profiles were coupled (term  $P$ ) to smooth the process along the 2D section made of all 1D vertical resistivity profiles. This coupling term minimizes the difference between the inversion result of the previous sounding and the current inverted sounding (see equation 1). The cost-function  $f_j$  for the current sounding  $j$  is expressed by:

$$f_j = M + \alpha \cdot R + \beta \cdot P \quad (1)$$

with  $M = \sum_i \frac{(\rho_{appmes_{i,j}} - \rho_{appcal_{i,j}})^2}{SD_{i,j}^2}$ ;  $R = \sum_i \frac{(\rho_{i,j} - \bar{\rho}_j)^2}{n_{layers}}$ ;  $P = \sum_i |\rho_{i,j} - \rho_{i,j-1}|^2$ , where  $i$  is the data index,  $\rho_{appmes_{i,j}}$  the apparent resistivity measured,  $\rho_{appcal_{i,j}}$  the calculated apparent resistivity,

$SD_{i,j}$  the standard deviation,  $\rho_{i,j}$  the model resistivity,  $\bar{\rho}_j$  the average resistivity value and  $\rho_{i,j-1}$  the resistivity of the previous inversion. The values  $\alpha$  and  $\beta$  are weighting coefficients. After several tests, the chosen coefficients were  $\alpha=0.0005$  and  $\beta=0.001$ . We used the 1D layering and the inversion parameters selected for the 2D inversion.

We then used a joint processing workflow between resistivity and P-wave velocity, which consisted in the addition of structural information from the seismic data into the inversion process. The coupling favoured resistivity models compatible with this *a priori* seismic information, a technique successfully tested on deep gas reservoirs (Du and Key 2018).

The velocity and the resistivity were coupled by a gradient correlation (Flamme *et al.* 2019). We added a coupling term between resistivity and velocity ( $S$ ) in the cost function (equation 2). This term is the product of the vertical derivatives of the velocity and the resistivity. The cost function becomes:

$$f_j = M + \alpha \cdot R + \beta \cdot P + \gamma \cdot S \quad (2)$$

with  $S = \left| 1 - \frac{(\sum_i (\nabla_{V_P} \times \nabla_{\rho}))^2}{\sum_i \nabla_{V_P}^2 \sum_i \nabla_{\rho}^2} \right|$ , where  $\nabla_{V_P}$  is the gradient of the P-wave velocity model and  $\nabla_{\rho}$  the gradient of the resistivity model.  $\gamma$  is a weighting coefficient.

## GEOPHYSICAL MODELS

### Acoustic amplitude and P-wave velocity

The seismic data were of excellent quality with an excellent signal to noise ratio (ambient noise due to currents and waves deleted, as well as artefacts and diffraction hyperbolas) and display the global variations of the stratigraphic organization (Figure 2b and Figure 3b). In the amplitude sections and outside the gas-bearing regions, paleo-incisions were clearly identified as well as the different geological units described by Jouet *et al.* (2019) using the simplified nomenclature proposed by Raimbault *et al.* (2018). The units are characterized by different P-wave interval velocities (Figure 2b) depending on the lithology (soft sediment or bedrock). Velocities are mainly determined by sediment texture (mean grain size) for unconsolidated marine sediment (Hamilton 1971; Kim 2006). Outside the gas-bearing regions, the seismic interpretation could provide a geological model shown in Figure 2a and Figure 3a.

### 2D resistivity models

We selected representative 2D resistivity models (lines MERT\_1, MERT\_2, MERT\_3 and MERT\_8, Figure 1, Figure 2c and Figure 3c), characterized by the presence of gas from seismic imaging and soft infilling sediment. The resistivity range ( $< 2 \Omega \cdot m$ ) is like other marine sedimentary environments (Tarits *et al.* 2012; Shankar and Riedel 2011; Garcia *et al.* 2014; Goswami *et al.* 2016). These values correspond to soft, porous, and saturated sedimentary deposits.

Overall, the resistivity distribution varies along with the geometry of the subsurface (Figure 2c and Figure 3c): successive sediment deposits (units U3 to U5) correspond to low resistivity values (between 0.5 and 0.9  $\Omega\cdot\text{m}$ ), whereas the rocky substratum (units U1 and U2) is characterised by higher resistivity values ( $>0.9 \Omega\cdot\text{m}$ ). Thus, the resistivity seems to be a discriminating factor of the geology. Average values of resistivity could then be attributed to the different geological units identified in the sections (Table 1).

Several sections show a shallow (a few meters BSF) heterogeneous upper layer in some places 2-3 times more resistive ( $\sim 1.5 \Omega\cdot\text{m}$ ) than underneath (Figure 2 and Figure 3), suggesting either an artefact in the processing or a variable composition in the layer. We carefully tested several inversion parameters that showed the same shallow resistive layer. This result supports the assumption that the shallow resistivity anomaly represents a real structure. Moreover, this resistivity anomaly forms a well-defined structure closest to the acquisition system.

### Geophysical signature of gas areas

#### In seismic data

Four major gas areas (areas 1 to 3 in Figure 2 and area 4 in Figure 3) were identified in the data and characterized by typical acoustic behaviours (Thi Van Ngo and Ferguson 2020): strong acoustic turbidity (gas blanking on seismic profiles, observed when the acoustic energy is scattered by gas bubbles) and high-amplitude reflection. The occurrence of free gas strongly reduced the penetration of the acoustic signal which is then limited to the gas caps 5 to 20 m BSF (areas 1 to 3 in Figure 2b and area 4 in Figure 3b). Free gas also altered the P-wave velocity  $V_p$ . The velocity drops from  $\sim 1600$  to 1400 m/s in area 2 down to  $\sim 1200$  m/s in area 3 (Figure 2b). The  $V_p$  values are similar to those obtained in similar gas-bearing marine environments (Seo, Kim and Park 2001; Shankar and Riedel 2011; Garcia *et al.* 2014; Kim *et al.* 2014).

#### In resistivity data

In free-gas areas, the resistivity models show the lowest resistivity values ( $\sim 0.5 \Omega\cdot\text{m}$ ; regions 1 to 4 in Figure 2 and Figure 3). This observation seems in contradiction with what is usually observed in other studies on similar gas-bearing marine environments, where an increase in resistivity values compared to the surrounding background resistivity is correlated to the presence of free gas (Lee *et al.* 2009 and Qian *et al.* 2018 in shallow contexts; Goswami *et al.* 2016 for a water depth of several hundreds of meters). The presence of gas (an electrical insulator) may tend to increase the resistivity of the bulk matrix because it may block or isolate the conductive water in the pores (Ren *et al.* 2010). However, other studies found resistivity decreasing on gas-bearing sediment like our observations and interpreted them in terms of porosity effect (Garcia *et al.* 2014). In our case, the presence of fine sediment such as silt and clay in gas-bearing sediments (Table 1) may also have a conductive effect (Long *et al.* 2012) and thus be responsible for low resistivity values. Yet, as low resistivity values also concern deeper layers devoid of silt and clay contents (units U3 and U4 in area

3, Figure 2), the conductive effect of fine particles may play a minor role. This observation suggests that high porosity can be the main factor explaining low resistivity values in our study area.

### 1D-constrained inversion

We compared the previous 2D sections and the new 2D sections in Figure 3c and Figure 3d for the MERT\_8 profile. The mean RMS of all individual 1D inversions was less than 1% (0.89% for line MERT\_8). Both 2D and 2D models are similar whilst we observed larger resistivity values for the 1D models compared to 2D results due to the differences in the inversion method.

The addition of the seismic constraint slightly increased the mean RMS (0.93% for line MERT\_8) but the latter remained low. In Figure 4, we present a study of the effect of increasing coupling. The RMS varied from 0.90 to 0.95% while the imprint of the seismic velocity structures becomes more and more apparent as the coupling increases. We also observe that the resistivity values tend to intensify with the coupling. Noteworthy, the salient features of the resistivity model were conserved (the uppermost resistive layer, the low resistivity zone of the gas region). However, at depths larger than  $\sim 10$  m BSF, the resistivity tends to adjust itself to several seismic structures. This observation suggests that among the acceptable inverse models in terms of misfits, some are clearly in agreement with the seismic layering outside the gas region. We selected the coupled resistivity model (Figure 3e) corresponding to a resistivity range like the model without coupling (no overshooting) and a small misfit increase. Thus, the  $\gamma$  value was fixed to 0.0004 in order to have a visible but moderate impact of the seismic constraint on the result.

## DISCUSSION

### On the 1D constrained inversion

We now discuss the ability of the tested 1D constrained inversion to bring new information on the geology. The section displayed in Figure 3 is an example with a strong acoustic blanking caused by free gas in the sediment (black dashed rectangle in Figure 3). Outside the gas zone, the shallow part is dominantly more resistive than the rest of the models (up to  $1.5 \Omega \cdot \text{m}$ ) while the velocity (Figure 3b) is the lowest ( $< 1600$  m/s). Deeper, the resistivity value decreases then increases again with depth (Figure 3e) whereas the P-wave velocity increases (Figure 3b). These contrasted behaviour between velocity and resistivity as a function of depth suggests different mechanisms on these parameters in the superficial sediments and in the deeper geological layers. In particular, the coupled 2D resistivity model (Figure 3e) showed structures remarkably similar to the seismic velocity, particularly at distances more than 1200 m. In contrast, at distances less than 1000 m, the coupled 2D resistivity model (Figure 3e) shows a more complicated pattern than beyond 1200 m. It seems that competing processes exist there and near the surface affecting the resistivity and velocity differently while in general agreement with the velocity and seismic amplitude horizons (Figure 3b).

In the gas zone (black rectangle in Figure 3), the masked seismic zone corresponds to a conductive region compared to areas on both sides of the resistivity models (Figure 3c, 3d and 3e). The coupling was not applied to this region (excepted to the top and sides where the velocity was obtained; Figure 3b). The base of the infilled paleovalley (Ux3 in Figure 3) containing gas could be guessed on the 2D model (Figure 3c) but was less visible in the 2D sections (Figure 3d and 3e). Yet, the 1D constrained resistivity model suggests a continuity of the deepest geological structures (area I in Figure 3e). We reached the same conclusions in all the other resistivity sections. This result could be obtained despite the absence of seismic data in the gas area because the better constraint on resistivity at each side of the gas area helped the inversion algorithm to converge towards resistivity models more coherent with the geometry of the geology, and thus the improvement of resistivity models where seismic data is available allows the improvement of resistivity models in masked areas if the seismic mask is not too wide.

Geological interfaces could then be guessed in the resistivity model, particularly when the depth increased (area II, Figure 3e). The shape of the superficial resistive layer (area I) was also better defined and followed the shape showed by the seismic data more precisely. These results suggest a promising method to improve geological knowledge in acoustic blanking areas.

### Quantitative joint analysis

#### Joint analysis of geophysical data (UHR $V_p$ and MERT resistivity)

As the constrained inversion is only a 1D approach and newly developed, we used the 2D inversion models obtained with Res2DInv to carry out the analysis of resistivity values and the quantitative comparison with seismic data and MSCL results.

In order to quantify the visual agreement between resistivity and seismic data, we investigated the relationship between P-wave velocity and resistivity and compared these data to MSCL results from cores near the geophysical sections. The values were reported in Figure 5 for the regions A, B and C defined in Figure 2e.

We observed two trends depending on the depth of burial of the sediments. Near the seabed (areas A and C), the resistivity increases whereas the P-wave velocity remains close to the sea water velocity. In contrast, in the deeper layers (area B), both P-wave velocity and resistivity increase. A polynomial regression identifies these two relationships between velocity and resistivity (Figure 5).

Porosity is the main controlling parameter for both resistivity and velocity for near seabed sediments (Hamilton and Bachman 1982; Garcia *et al.* 2014). Water content and porosity decrease with depth because of compaction and consolidation (Mosher, Moran and Hiscott 1994) which would explain the trend observed in region B (Figure 5) and hence the difference with the seabed sediments.

The resistivity and velocity values in area C above the gas bearing sediments were the smallest (Figure 5). The near seabed values agreed with the values in area A. However, closer to the gas-bearing sediments (Figure 2), the  $V_p$  values drop significantly (down to 1300 m/s) while the resistivity remains about constant ( $\sim 0.6 \Omega.m$ ).

### Study of the MSCL data

The robustness and scale of both the drop of  $V_p$  values and the steadiness of resistivity values near the seabed can be tested at the core sampling scale. Three cores (KS33, KS02, and KS32 in Figure 1 and Figure 2) were located on the geophysical lines (Table 2). We reported the MSCL  $V_p$  values as a function of depth for each core in Figure 6a. Between 0-1.5 m BSF, the velocity was similar in all three cores ( $\sim 1500$  m/s). In cores KS02 and KS32,  $V_p$  increased with depth from 1400 to 1600 m/s. In core KS33, located in gas region 2 (see Figure 2), we observe a drop in  $V_p$  ( $\sim 1250$  m/s) at 2.1 m BSF (Figure 6a). This is typical of gas-bearing marine sediment and has also been observed on the geophysical data (Figure 2b) and at similar depths in other studies (*e.g.*, Lee *et al.* 2009).

The MSCL porosity measured along with  $V_p$  is  $\sim 75\%$  in the first meter BSF for all three cores (Figure 6b). These values were like other areas presenting fine and muddy sediment (Seo *et al.* 2001; Kim *et al.* 2014), with porosity ranging between 72 and 81%. From 1 to 4 m BSF, the porosity decreased (40-70%). For this depth range, the highest values ( $\sim 60-70\%$ ) were obtained in core KS33 (Figure 6b) in gas region 2 (Figure 2). This observation could suggest a high porosity in the gas-bearing sediment.

For the three cores studied, we plotted the MSCL  $V_p$  as a function of porosity (Figure 7). We calculated a polynomial regression for comparison with other studies. Our polynomial law laid between that of Hamilton and Bachman (1982), and Liu *et al.* (2013) (Figure 7). Our relationship fitted Hou *et al.* (2018) and Anderson (1974) very well. Both studies are for gas free sediments, suggesting that regions outside gas areas in the Bay of Concarneau were gas-free sediments in agreement with the analysis by Baltzer *et al.* (2014). In contrast, the MSCL velocity from core KS33 in the gas region 2 described in Figure 2 was less than for KS02 and KS32 (1200-1400 m/s) with a fairly stable porosity of 60-70% (Figure 7).

### Porosity from MERT resistivity

Having 2D resistivity models, it is possible to evaluate a 2D connected-porosity model at the geophysical scale using the Archie's law (Archie 1942; Garcia *et al.* 2014). This would also allow a closer comparison between MERT data and MSCL data, as no resistivity measurements were performed on cores with the MSCL bench. If the Archie's law can be directly used for non-gas-bearing sediments (*i.e.*, most part of our lines), it is not the case for gas-bearing sediments (areas showing acoustic masks) if the gas content is not negligible.

The Archie's law can either use the gas saturation or assume full water saturation of the pore space (Garcia *et al.* 2014). To choose the most appropriate version of the relation, we must evaluate the gas content in the sediment, and if it is necessary to take it into account in the porosity calculation of the sediment.

First, we investigate the gas dissolution in the seawater to rigorously evaluate the resistivity of the pore fluid. As no pore-fluid analysis was conducted on the studied cores (KS33, KS02 and KS32), we do not have values of methane content in the pore fluid at the location of our geophysical lines.

However, pore-fluid analysis was carried out on other cores extracted in the Bay of Concarneau (Baltzer *et al.* 2014). The results showed very low content of dissolved methane (0.04%, corresponding to a maximum measured concentration of 400  $\mu\text{L/L}$ ). It is negligible compared to other ion contents, such as NaCl. These observations agree with the low dissolution rate of methane in seawater (Yamamoto, Alcauskas and Crozier 1976). From these arguments, it is reasonable to assume that the ionic capacity of the pore fluid is marginally modified by methane and can still be assimilated to seawater. Moreover, the presence of gas bubbles revealed by acoustic masks proves that the methane solubility has been exceeded.

Second, we investigate the possible pore space filled with gas bubbles. Several authors (Holbrook *et al.* 1996; Ecker, Dvorkin and Nur 2000) showed that only 1% of the pore space filled with gas is enough to create an acoustic mask, whereas this is not enough to have a clear resistive effect on MERT data. Some studies, realized in similar geological contexts, evaluated the gas content in the sediment using mainly seismic data. At this shallow depth, the bulk modulus of the gas is so low that a very small amount of gas enables to drop dramatically the P-wave velocity. Toth *et al.* (2014) found that even very small amounts of gas cause a significant decrease in the compressional wave velocity. For instance, a 50% drop in P-wave velocity is associated to 0.1% gas volume. They also associated a drop of 300 m/s to  $\sim 0.03\%$  of gas, and a drop of 500 m/s to  $\sim 0.07\%$  of gas. In our case, the velocity drop over gas areas is between 200 and 400 m/s (Figure 2b), which can correspond to gas volumes of 0.02 to 0.05 % according to Toth *et al.* (2014). These values are very low and certainly have no impact on resistivity measurements.

Besides, we observed in our study area that free gas had no resistive effect on the resistivity models, showing on the contrary systematically a more conductive sediment (Figure 2c and Figure 3c). All these arguments suggest that in the Bay of Concarneau, free gas is not the factor explaining resistivity variations, and thus it is reasonable to neglect its content in the Archie's law. The porosity calculation can then be carried out using the following expression:

$$\phi = \left( a \frac{\rho_w}{\rho_t} \right)^{1/m} \times 100 \quad (3)$$

where  $\phi$  is the connected porosity (%),  $\rho_t$  the *in situ* bulk resistivity ( $\Omega\cdot\text{m}$ ),  $\rho_w$  the seawater resistivity inferred from CTD profiles and set to 0.25  $\Omega\cdot\text{m}$ ,  $m$  the cementation factor usually ranging between 1.8 and 2,  $a$  the tortuosity factor usually close to 1.

Lee and Collett (2006) evaluated for marine sediments the values of  $a$  and  $m$  for several clay contents. Their results are usable for porosity values higher than  $\sim 10\%$  and if there is a linear relationship between the logarithms of the resistivity and the porosity. In our study area, these conditions are at least fulfilled for superficial sediments according to core data (Figure 8). No precise value of clay content was available on the geophysical lines, but geological observations on cores showed that the sediment is fine and muddy, mainly composed of silt. We synthesized the MERT resistivity and the MSCL porosity and determined the  $a$  and  $m$  values that fitted the best both MERT and MSCL data for the range studied by Lee and Collett (2006). We obtained  $a = 1.06$  and  $m = 1.79$ . As the gas content is not considered in this equation, it is more careful to consider the

calculated porosity as the minimum connected porosity, the true porosity (*i.e.*, connected and non-connected pores) being certainly slightly higher.

The vertical profiles of porosity in Figure 6e were inferred from the MERT resistivity profiles (Figure 6d) extracted from the MERT model (Figure 2c) the nearest from the core locations. The MERT porosity (Figure 6e) and the MSCL porosity (Figure 6b) had similar values (45-65%) deeper than 1.5 m BSF. Yet, the difference between MSCL and MERT porosity increased close to the seabed (within 1-1.5 m) because the vertical resolution of the MERT data was more than 1-1.5 m, reflecting the huge difference of scales between geotechnical and geophysical data. The porosity inferred from MERT data (Figure 6e) could hardly detect thin layers, whereas geotechnical data could distinguish them more easily.

We applied the Archie's law to the full MERT section with the parameters obtained (Figure 2d). To validate the MERT porosity (deduced from the Archie's law), we reported in Figure 9 for areas C, D, E, F (Figure 2f) the UHR seismic P-wave velocity as a function of the MERT porosity, which is equivalent to Figure 5 but for different areas of the geophysical section (Figure 2f). We reported in Figure 9 the polynomial regression for the MSCL data (black solid line) shown in Figure 7. For the depth range covered by the core data (0-5 m BSF), the law was in very good agreement with the geophysical data distribution (Figure 9). Outside the regions with gas-bearing sediments, the geophysical and geotechnical data agree despite their considerably different scale. As in Figure 5, only the data from the region with gas-bearing sediment departed from the trends because the velocity is no longer primarily controlled by the porosity (Kim *et al.* 2014).

The MERT porosity varied along with geological units and thus seemed to be a discriminating factor of the geology. We could attribute ranges of porosity values to the different geological units (Table 1) identified in Figure 2a.

#### Porosity in the gas-bearing sediment

In gas-bearing sediment regions (black rectangles in Figure 2 and Figure 3), the masked seismic zone is electrically conductive compared to both sides of the resistivity models (Figure 2c and Figure 3c). In Figure 2 and Figure 3 and in the vertical profiles (Figure 6e), the porosity computed from the Archie's law validated outside the gas-bearing sediments at depths more than ~5 m BSF was larger (60-70%) in the gas-bearing sediments than anywhere else. In similar studies (Lee *et al.* 2009; Goswami *et al.* 2016; Garcia *et al.* 2014; Vargas-Cordero *et al.* 2018), the porosity of superficial Holocene gas-bearing sediment ranges between 50-75%, which agrees with our data. In our study, we could precise the porosity interval boundaries for gas-bearing sediments in the Bay of Concarneau. The obtained values correspond to high porosities. This seems to validate the hypothesis made by Boudreau *et al.* (2005) that free gas accumulation in the sediment may fracture the cohesive host medium or reopen pre-existing fractures. These failures could be responsible for the increase of the porosity of the gas-bearing sediments and explain our results. Likewise, computer simulations suggest that sediment fracturing may also trigger bubble rise (Algar *et al.* 2011), and thus measuring the sediment porosity may directly lead to gas migration and pathways localization.

## CONCLUSION

We presented results of an integration of high resolution geophysical and geotechnical data sets to characterize gas bearing sediments in the Bay of Concarneau. The proposed integrated processing workflow showed the complementarity relationship between seismic and resistivity imaging in the case of shallow gas-bearing sediments. Indeed, seismic data provide information on the soil interfaces outside of gas areas, which can be used to improve the inversion of apparent resistivity values, whereas resistivity variations bring additional geometry information in areas with seismic acoustic blanking. However, a 2D constrained inversion would probably improve the resolution within the gas zone better than the 1D constrained inversion. The global analysis of the available data suggested a low gas content in the sediment despite the strong acoustic signature of free gas. Outside seismic masked regions, we found different relationships between velocity and resistivity for near seabed (1-5 m BSF) and deeper sediments (5-25 m BSF). Near seabed, the relationship was  $V_p = 176.09\rho^2 - 94.09\rho + 1567.7$  ( $R^2=0.66$ ); while deeper, this relationship became  $V_p = 1390.16\rho + 764.94$  ( $R^2=0.64$ ). In a second step, the established relationship between  $V_p$  and the porosity inferred from the resistivity models using the Archie law showed a very good agreement with geotechnical data: the UHR velocity-MERT porosity relationship ( $V_p = 1.19\phi^2 - 165.39\phi + 7034.19$ ;  $R^2=0.70$ ) was found to be very similar to the MSCL velocity-porosity relationship ( $V_p = 0.25\phi^2 - 34.15\phi + 2658.3$ ;  $R^2=0.67$ ). These relationships demonstrated the validity of MERT resistivity as a proxy for porosity both at geophysical and geotechnical scales. As a result, we could deduce with good confidence the porosity at the MERT scale for the entire survey lines, including regions of gas-bearing sediment, where the porosity was found to be  $\sim 0.5$   $\Omega$ .m. Thus, MERT jointly with seismic data may be a useful tool to refine the lithology and map porosity variations throughout geological structures including gas-bearing sediments.

### *Data Availability Statement*

The data that support the findings of this study are available from the corresponding author upon reasonable request.

### *References*

- Algar C. K., Boudreau B. P. and Barry M. A. 2011. Initial rise of bubbles in cohesive sediments by a process of viscoelastic fracture. *Journal of Geophysical Research: Solid Earth*, 116(B4).
- Anderson R. S. 1974. Statistical correlation of physical properties and sound velocity in sediments. In *Physics of sound in marine sediments*, 481-518. Springer, Boston, MA.
- Anderson A. L. and Hampton L. D. 1980. Acoustics of gas-bearing sediments I. Background. *The Journal of the Acoustical Society of America*, 67(6), 1865-1889.

- Archie G. E. 1942. The electrical resistivity log as an aid in determining some reservoir characteristics. *Transactions of the American Institute of Mining Metallurgical and Petroleum Engineers*, 146(01), 54-62.
- Baltzer A., Ehrhold A., Rigolet C., Souron A., Cordier C., Clouet H. and Dubois S. F. 2014. Geophysical exploration of an active pockmark field in the Bay of Concarneau, southern Brittany, and implications for resident suspension feeders. *Geo-Marine Letters*, 34(2-3), 215-230.
- Baltzer A., Reynaud M., Ehrhold A., Fournier J., Cordier C. and Clouet H. 2017. Space-time evolution of a large field of pockmarks in the Bay of Concarneau (NW Brittany) Évolution spatio-temporelle d'un champ de pockmarks dans la Baie de Concarneau (Nord-Ouest de la Bretagne). *Bulletin de la Société géologique de France*, 188(4).
- Boudreau B. P., Algar C., Johnson B. D., Croudace I., Reed A., Furukawa Y., Dorgan K. M., Jumars P. A., Grader A. S. and Gardiner B. S. 2005. Bubble growth and rise in soft sediments. *Geology*, 33(6), 517-520.
- Constable S., Kannberg P. K. and Weitemeyer K. 2016. Vulcan: A deep-towed CSEM receiver. *Geochemistry, Geophysics, Geosystems*, 17(3), 1042-1064.
- Das B. M. and Sivakugan N. 2016. *Fundamentals of geotechnical engineering*. Cengage Learning.
- Delanoë Y. and Pinot J. 1977. Littoraux et vallées holocènes submergés en Baie de Concarneau (Bretagne méridionale). *Quaternaire*, 14(3), 27-38.
- Deming D. 2004. Can a single bubble sink a ship? *Journal of Scientific Exploration*, 18(2), 307–312.
- Du Z. and Key K. 2018. Case study: North Sea heavy oil reservoir characterization from integrated analysis of towed-streamer EM and dual-sensor seismic data. *The Leading Edge*, 37(8), 608-615.
- Ecker C., Dvorkin J. and Nur A. M. 2000. Estimating the amount of gas hydrate and free gas from marine seismic data. *Geophysics*, 65(2), 565-573.
- Ehrhold A., Hamon D. and Guillaumont B. 2006. The REBENT monitoring network, a spatially integrated, acoustic approach to surveying nearshore macrobenthic habitats: application to the Bay of Concarneau (South Brittany, France). *ICES Journal of Marine Science*, 63(9), 1604-1615.
- Ehrhold A. and Riboulot V. 2018. SYPOCO Campaign cruise, RV Thalia. <https://doi.org/10.17600/18000420>
- Flamme J., Fabre M., Tarits P., Marsset B. and Lepot A. 2019. Combining marine electromagnetic and high-resolution seismic imaging: application to shallow gassy environment. In *SAGEEP 2019* (Vol. 2019, No. 1, pp. 1-4). European Association of Geoscientists & Engineers.
- Fleischer P., Orsi T., Richardson M. and Anderson A. 2001. Distribution of free gas in marine sediments: a global overview. *Geo-Marine Letters*, 21(2), 103-122.

- Garcia X., Monteys X., Evans R. L. and Szpak M. 2014. Constraints on a shallow offshore gas environment determined by a multidisciplinary geophysical approach: The Malin Sea, NW Ireland. *Geochemistry, Geophysics, Geosystems*, 15(4), 867-885.
- Gardner T. N. 2000. An acoustic study of soils that model seabed sediments containing gas bubbles. *The Journal of the Acoustical Society of America*, 107(1), 163-176.
- Goswami B. K., Weitemeyer K. A., Minshull T. A., Sinha M. C., Westbrook G. K. and Marín-Moreno H. 2016. Resistivity image beneath an area of active methane seeps in the west Svalbard continental slope. *Geophysical Supplements to the Monthly Notices of the Royal Astronomical Society*, 207(2), 1286-1302.
- Hamilton E. L. 1971. Prediction of in situ acoustic and elastic properties of marine sediments. *Geophysics*, 36(2), 266-284.
- Hamilton E. L. and Bachman R. T. 1982. Sound velocity and related properties of marine sediments. *The Journal of the Acoustical Society of America*, 72(6), 1891-1904.
- Holbrook W. S., Hoskins H., Wood W. T., Stephen R. A. and Lizarralde D. 1996. Methane hydrate and free gas on the Blake Ridge from vertical seismic profiling. *Science*, 273(5283), 1840-1843.
- Hou Z., Chen Z., Wang J., Zheng X., Yan W., Tian Y. and Luo Y. 2018. Acoustic impedance properties of seafloor sediments off the coast of Southeastern Hainan, South China Sea. *Journal of Asian Earth Sciences*, 154, 1-7.
- Hovland M. and Judd A. G. 1992. The global production of methane from shallow submarine sources. *Continental Shelf Research*, 12(10), 1231-1238.
- Jouet G., Ehrhold A., Riboulot V., Belleney D., Sommer-Delfolie S., Baltzer A., Dupont P., Fabre M., Le Roy P., Marches E., Thomas Y. and Schmidt S. 2019. Late Holocene sedimentation in the Bay of Concarneau (South-Western Brittany, France); implications for interstitial fluid circulations. *17ème Congrès Français de Sédimentologie (ASF)*, Beauvais, France, 22-24 octobre 2019 Publ. ASF n°81, Paris, 169 p.
- Jovanovich D. B., Sumner R. D. and Akins-Easterlin S. L. 1983. Ghosting and marine signature deconvolution: A prerequisite for detailed seismic interpretation. *Geophysics*, 48(11), 1468-1485.
- Judd A. and Hovland M. 2009. *Seabed fluid flow: the impact on geology, biology and the marine environment*. Cambridge University Press.
- Kim G. Y. 2006. Acoustic and elastic properties of the southeastern Yellow Sea Mud, Korea. *The Journal of the Acoustical Society of Korea*, 25(2E), 49-55.
- Kim G. Y., Narantsetseg B., Kim J. W. and Chun J. H. 2014. Physical properties and micro-and macro-structures of gassy sediments in the inner shelf of SE Korea. *Quaternary International*, 344, 170-180.

- Lee M. W. and Collett T. S. 2006. *A method of shaly sand correction for estimating gas hydrate saturations using downhole electrical resistivity log data* (Vol. 5121). US Department of the Interior, US Geological Survey.
- Lee G. S., Kim D. C., Lee G. H., Park S. C., Kim G. Y., Yoo D. G., Kim J.-C. and Cifci G. 2009. Physical and acoustic properties of gas-bearing sediments in Jinhae Bay, the South Sea of Korea. *Marine Georesources and Geotechnology*, 27(2), 96-114.
- Liu B., Han T., Kan G. and Li G. 2013. Correlations between the in situ acoustic properties and geotechnical parameters of sediments in the Yellow Sea, China. *Journal of Asian Earth Sciences*, 77, 83-90.
- Loke M. H. 2004. Tutorial: 2-D and 3-D electrical imaging surveys.
- Loke M. H. 2016. RES2DINV version 6.1. Geoelectrical Imaging 2D and 3D. Instruction Manual. Geotomo Software.
- Long M., Donohue S., L'Heureux J. S., Solberg I. L., Rønning J. S., Limacher, R., O'Connor P., Sauvin G., Rømøen M. and Lecomte I. 2012. Relationship between electrical resistivity and basic geotechnical parameters for marine clays. *Canadian Geotechnical Journal*, 49(10), 1158-1168.
- Marsset B. 2016. ESS\_FLUTE PLATEAU cruise, RV Thalia, <https://doi.org/10.17600/16006200>
- Martens C. S. and Klump J. V. 1980. Biogeochemical cycling in an organic-rich coastal marine basin—I. Methane sediment-water exchange processes. *Geochimica et Cosmochimica Acta*, 44(3), 471-490.
- Menier D. 2003. Morphologie et remplissage des vallées fossiles sud-armoricaines: apports de la stratigraphie sismique (Doctoral dissertation, Lorient).
- Menier D., Reynaud J. Y., Proust J. N., Guillocheau F., Guennoc P., Bonnet S., Tessier B. and Goubert E. 2006. Basement control on shaping and infilling of valleys incised at the southern coast of Brittany, France. *SEPM special publications*, 85, 37-55.
- Mosher D. C., Moran K. and Hiscott R. N. 1994. Late Quaternary sediment, sediment mass flow processes and slope stability on the Scotian Slope, Canada. *Sedimentology*, 41(5), 1039-1061.
- Pinot J. P. 1974. *Le précontinent breton entre Pen Marc'h, Belle-Ile et l'escarpement continental: étude géomorphologique. Etat des travaux au 1° novembre 1972. 1° éd* (Doctoral dissertation).
- Prince, P. K. 1990. Current drilling practice and the occurrence of shallow gas. In *Safety in Offshore Drilling* (pp. 3-25). Springer, Dordrecht.
- Qian J., Wang X., Collett T. S., Guo Y., Kang D. and Jin J. 2018. Downhole log evidence for the coexistence of structure II gas hydrate and free gas below the bottom-simulating reflector in the South China Sea. *Marine and Petroleum Geology*, 98, 662-674.

- Raimbault C., Duperret A., Le Gall B. and Authemayou C. 2018. Structural inheritance and coastal geomorphology in SW Brittany, France: An onshore/offshore integrated approach. *Geomorphology*, 306, 141-154.
- Ren S. R., Liu Y., Liu Y. and Zhang W. 2010. Acoustic velocity and electrical resistance of hydrate bearing sediments. *Journal of Petroleum Science and Engineering*, 70(1-2), 52-56.
- Rice D. D. and Claypool G. E. 1981. Generation, accumulation, and resource potential of biogenic gas. *AAPG bulletin*, 65(1), 5-25.
- Seo Y. K., Kim D. C. and Park S. C. 2001. Characteristics of Velocity and Electrical Resistivity in Gassy Sediments Results of Mudbelt Sediments in the Southeastern Inner Shelf of Korea. *The Sea*, 6(4), 249-258.
- Shankar U. and Riedel M. 2011. Gas hydrate saturation in the Krishna–Godavari basin from P-wave velocity and electrical resistivity logs. *Marine and Petroleum Geology*, 28(10), 1768-1778.
- Sharma S. and Verma G. K. 2015. Inversion of electrical resistivity data: a review. *International Journal of Computer and Systems Engineering*, 9(4), 400-406.
- Sills G. C. and Wheeler S. J. 1992. The significance of gas for offshore operations. *Continental Shelf Research*, 12(10), 1239-1250.
- Sultan N., Voisset M., Marsset T., Vernant A. M., Cauquil E., Colliat J. L. and Curinier V. 2007. Detection of free gas and gas hydrate based on 3D seismic data and cone penetration testing: An example from the Nigerian Continental Slope. *Marine Geology*, 240(1-4), 235-255.
- Tarits P., D'Eu J. F., Balem K., Hautot S., Prevot J. and Gaspari F. 2012. Mapping seismically masked seabed structures with a new DC resistivity streamer. In *Near Surface Geoscience 2012–18th European Meeting of Environmental and Engineering Geophysics* (pp. cp-306). European Association of Geoscientists & Engineers.
- Thi Van Ngo A. T. and Ferguson A. J. 2020. Identifying shallow gas zones by using seismic attributes, offshore Vietnam. *Interpretation*, 8(1), T67-T76.
- Toth Z., Spiess V., Mogollon J. M. and Jensen J. B. 2014. Estimating the free gas content in Baltic Sea sediments using compressional wave velocity from marine seismic data. *Journal of geophysical research: solid earth*, 119(12), 8577-8593.
- Vargas-Cordero I., Tinivella U., Villar-Muñoz L. and Bento J. P. 2018. High gas hydrate and free gas concentrations: An explanation for seeps offshore South Mocha Island. *Energies*, 11(11), 3062.
- Wilkens R. H. and Richardson M. D. 1998. The influence of gas bubbles on sediment acoustic properties: in situ, laboratory, and theoretical results from Eckernförde Bay, Baltic Sea. *Continental Shelf Research*, 18(14-15), 1859-1892.
- Yamamoto S., Alcauskas J. B. and Crozier T. E. 1976. Solubility of methane in distilled water and seawater. *Journal of Chemical and Engineering Data*, 21(1), 78-80.

Tables (with title and footnotes)

**Table 1: Summary of physical characteristics of the different geological units in the Bay of Concarneau described by Jouet *et al.* (2019) using the simplified nomenclature by Raimbault *et al.* (2018).**

Geological unit	Geological description / sediment type	P-wave velocity $V_P$ [m/s]	Resistivity $\rho$ [ $\Omega \cdot m$ ]	Porosity $\phi$ [%]
Acoustic mask/gas-bearing sediment	Masked unit, gas-bearing sediment at the top of the blanking areas; fine and organic-rich sediments (mud, silt, clay)	1100 ~ 1500	0.4 ~ 0.7	60 ~ 72
U1	Micaschist and gneiss, granitic basement	> 2100	> 1.15	< 42
U2	Eocene substratum; Bartonian nummulites limestone	1800 ~ 2800	0.8 ~ 1.3	37 ~ 49
U3	Oligocene coarse fluvial continental deposits	1500 ~ 1900	0.6 ~ 0.7	49 ~ 53
U4	Pleistocene estuarine tidal bars	1500 ~ 1900	0.6 ~ 1.0	49 ~ 72
U5	Holocene mud and sand	1400 ~ 1700	0.5 ~ 0.9	54 ~ 66

**Table 2: Minimum distance between the SYPOCO-KS33, SYPOCO-KS02, SYPOCO-KS32 core locations and geophysical survey lines ESS\_FLUTE\_11 and MERT\_2.**

Core	Distance to ESS_FLUTE_11 [m]	Distance to MERT_2 [m]	Length of cores [m]
SYPOCO-KS33	3.75	20.49	4.10
SYPOCO-KS02	13.19	26.18	3.72
SYPOCO-KS32	1.99	28.17	4.15

Figures

Figure 1

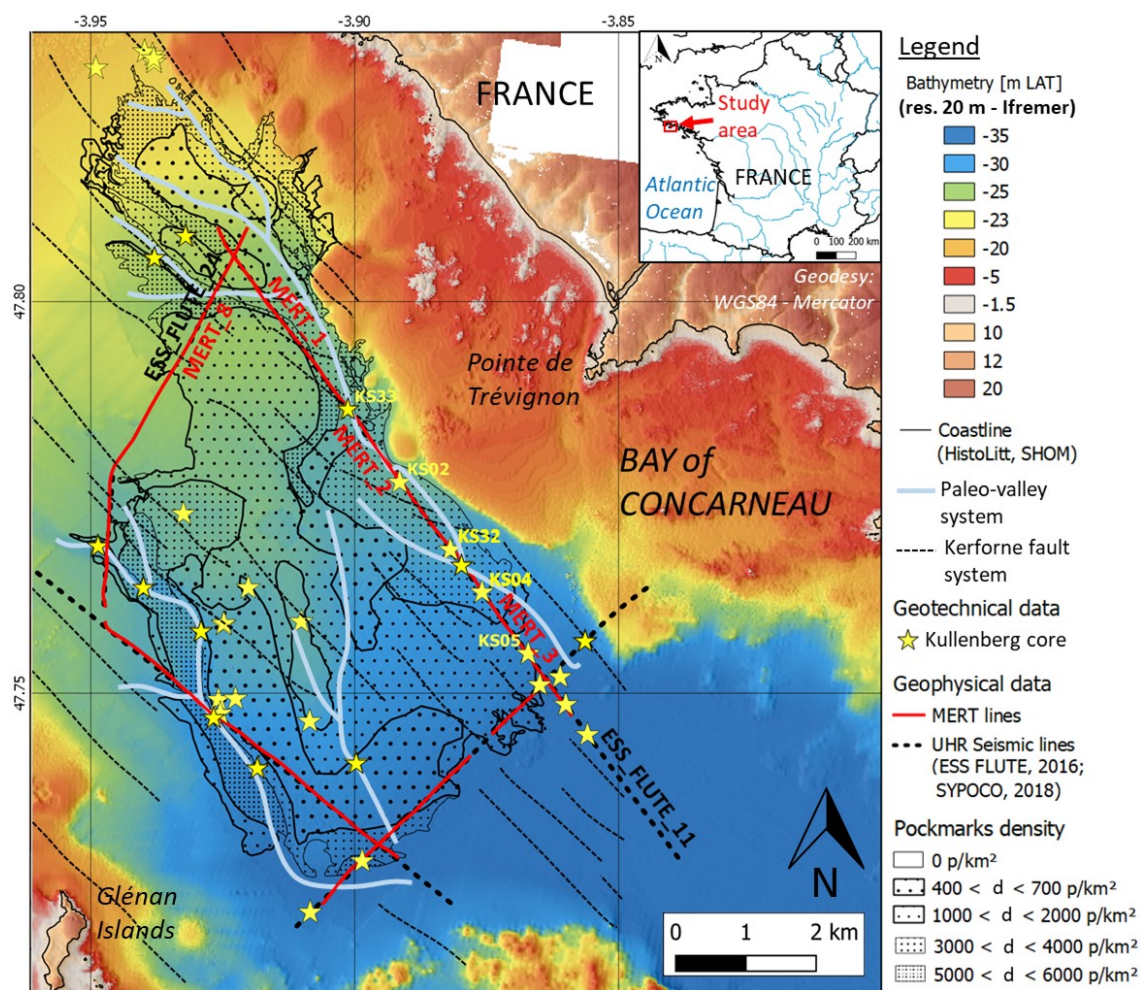
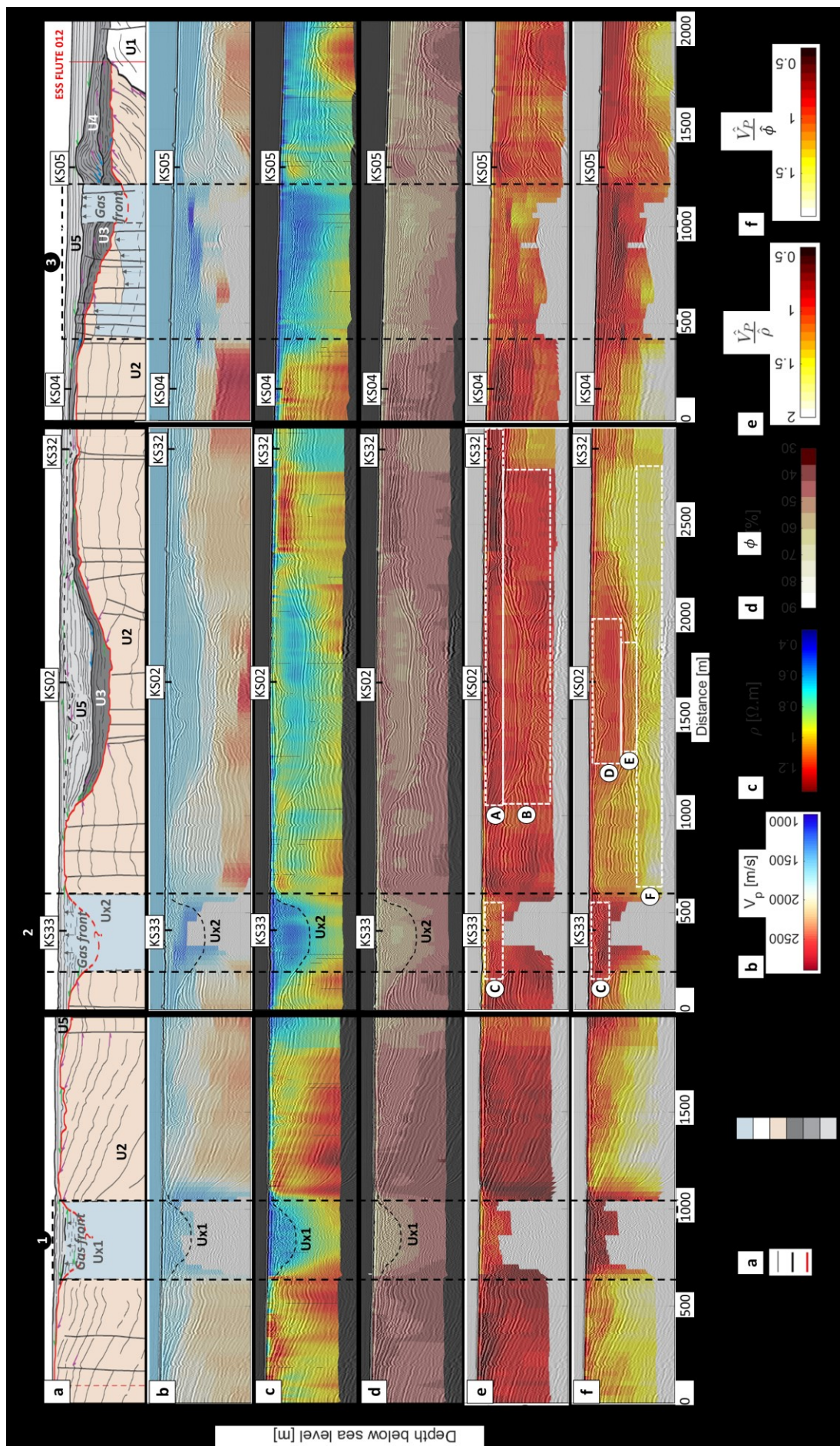


Figure 2





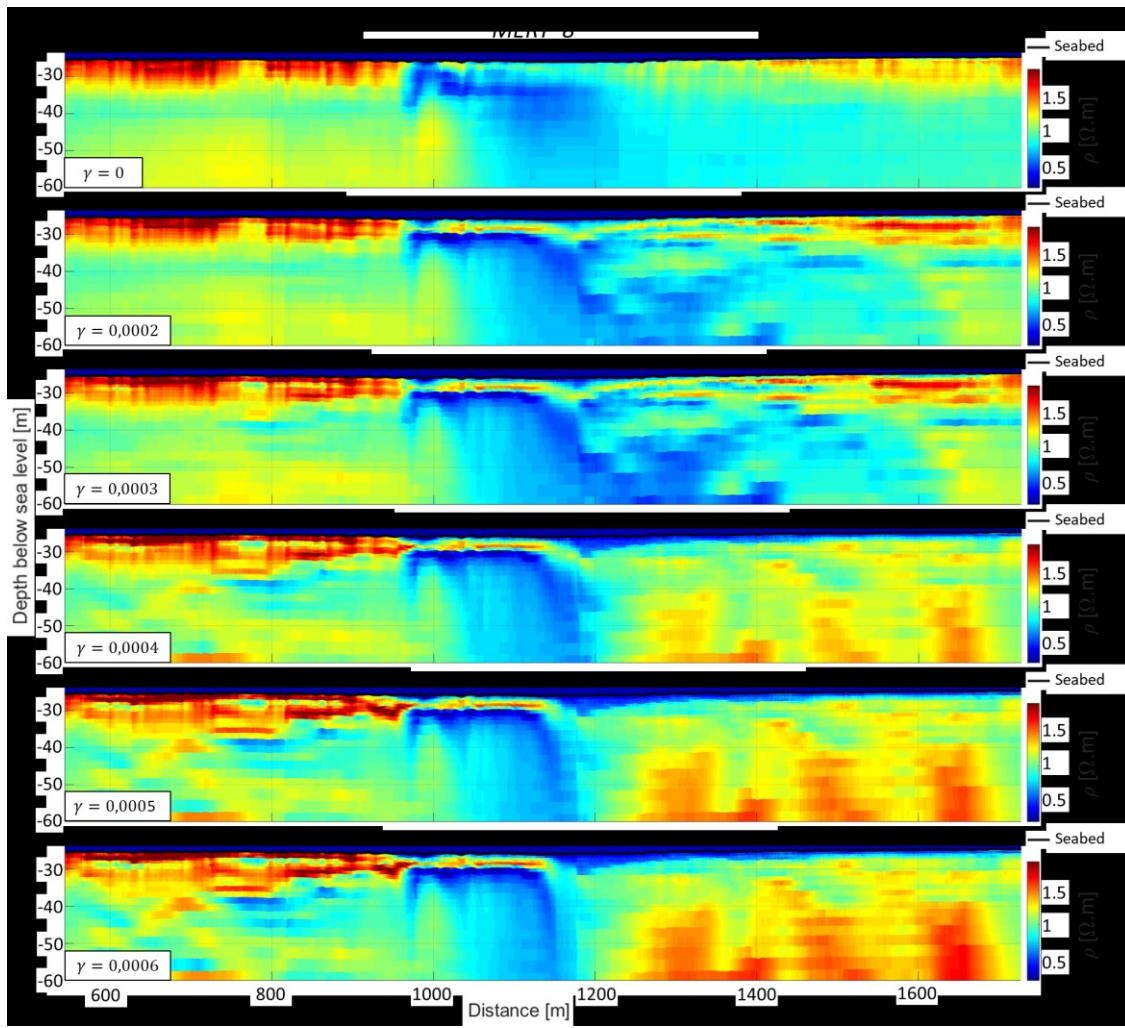


Figure 5

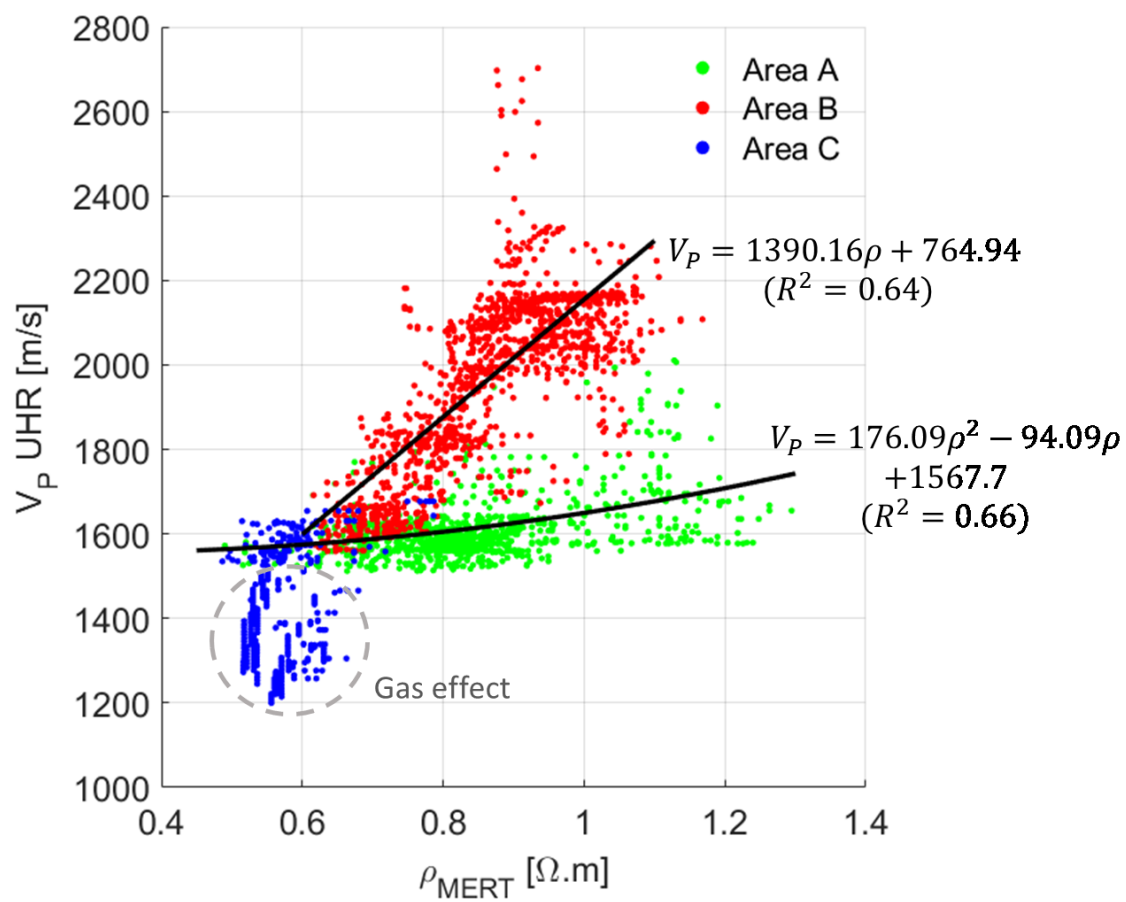


Figure 6

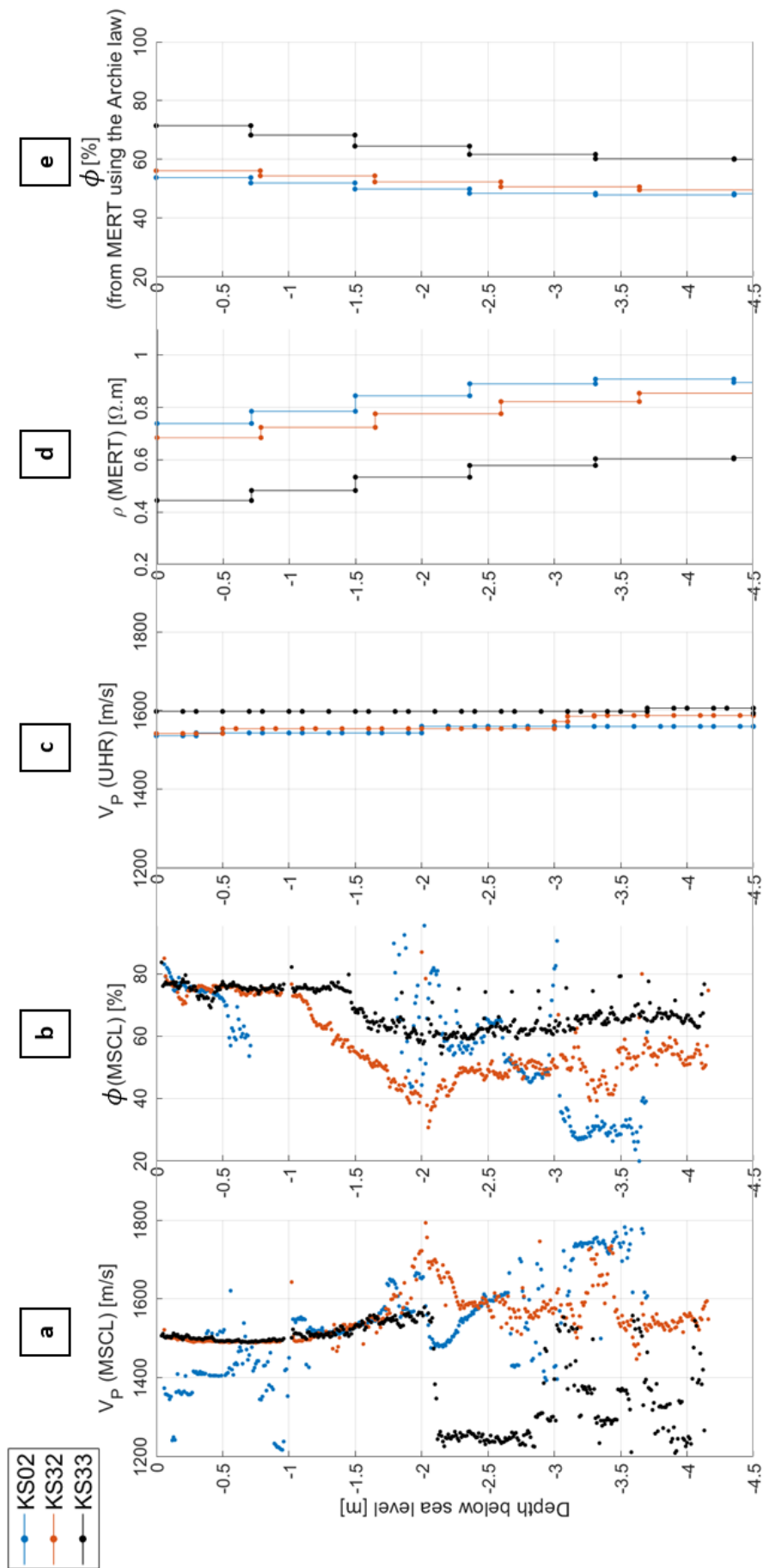


Figure 7

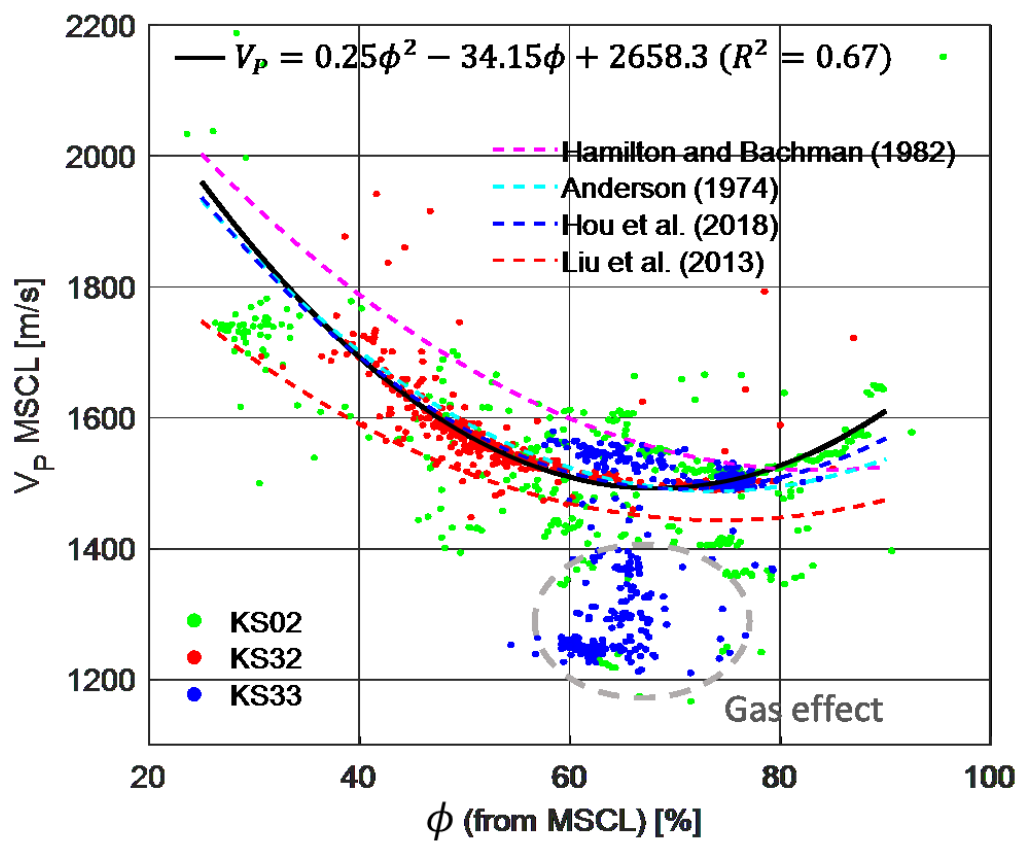


Figure 8

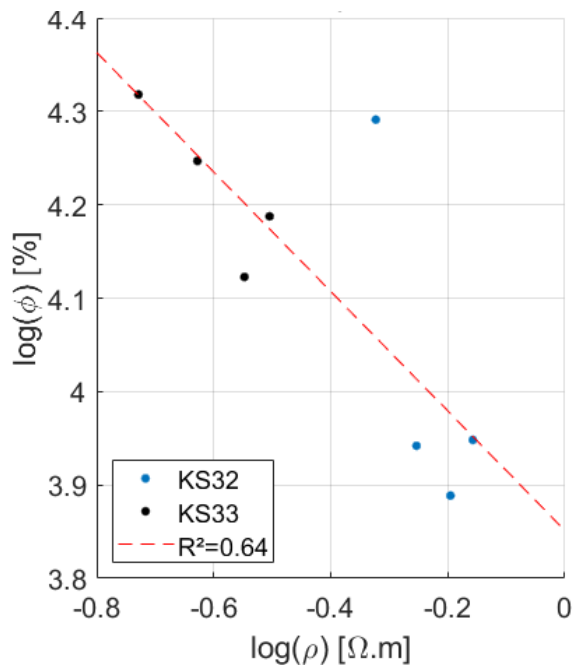
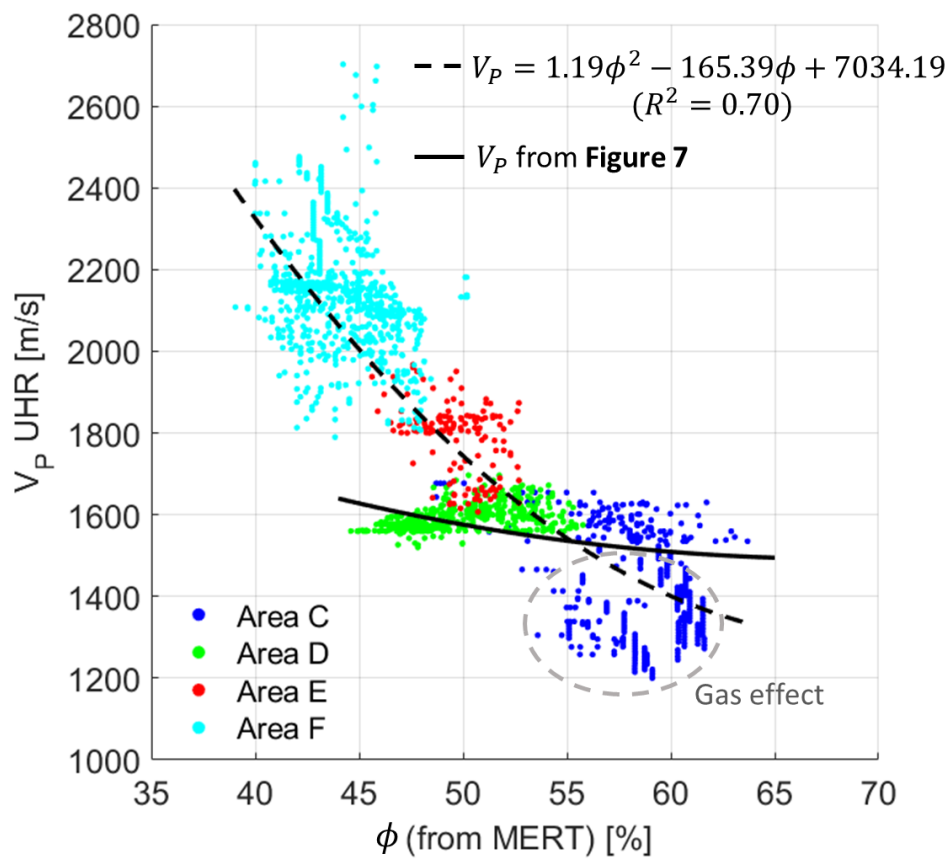


Figure 9



*Figure captions*

**Figure 1:** Map of the study area, displaying the geophysical survey lines (in red) and the location of the geotechnical data collected (yellow stars). The bathymetry is from Ifremer; the pockmarks density is from Baltzer et al. (2014) modified and completed by Riboulot (unpublished data).

**Figure 2:** Geology and geophysical sections for the seismic line ESS\_FLUTE\_11 and MERT lines MERT\_1, MERT\_2 and MERT\_3 (Figure 1). Each section shows the location of cores SYPOCO-KS33, SYPOCO-KS02 and SYPOCO-KS32. Areas 1-3 (black dashed rectangles) correspond to seismic masks because of free gas. The terms Ux1 and Ux2 are the proposed location of the paleo-valley bottom based on resistivity data. All sections (a-f) are superimposed on the seismic amplitude sections. (a) Geological interpretation based on the seismic interfaces in the acoustic amplitude. The red interface corresponds to the boundary between underlying rocky basement and overlying unconsolidated sediments. The geological units U1-U5 are described in the text. (b) P-wave velocity. The grey zones correspond to the seismic mask (areas 1-3). (c) Resistivity models obtained with Res2DInv. (d) Porosity inferred from the resistivity values, using the Archie law with parameters described in the text. (e) Ratio of normalized P-wave velocity ( $\widehat{V}_P = V_P/\overline{V}_P$ ) over normalized resistivity ( $\widehat{\rho} = \rho/\overline{\rho}$ ) interpolated on the P-wave velocity grid. The white rectangles A, B and C define three regions of different velocity and resistivity in Figure 5 (see text for details). (f) Ratio between normalized P-wave velocity and normalized porosity. The white rectangles C, D, E and F define four regions of different velocity and porosity in Figure 9 (see text for details). They correspond to different geological layers (respectively gas-bearing sediment, U3, U2 and U0).

Figure 3: Example of the 1D constrained inversion on seismic line ESS\_FLUTE\_24 and MERT line MERT\_8. The dashed black rectangle highlights the acoustic mask areas. All sections (a-e) are superimposed on the seismic amplitude sections. (a) Geological section based on the acoustic amplitude results (see text for details). (b) P-wave velocity model. (c) 2D resistivity model. (d) 2D resistivity model from 1D inversion. (e) 2D resistivity model from 1D inversion constrained by the velocity. The white rectangles I-III define three regions of different velocity and resistivity (see text for details).

Figure 4: 2D section of 1D inversions constrained by the velocity. From top to bottom, we increased the weight on the velocity model (equation 2).

Figure 5: UHR P-wave velocity as a function of the MERT resistivity for areas A, B and C (Figure 2e). The two trends (one for area A, other for area B) are evaluated using polynomial regressions (black solid lines). The grey dashed circle surrounds the values above the seismic mask zone.

Figure 6: Comparison between geotechnical and geophysical data for three cores (SYPOCO-KS32, SYPOCO-KS02 and SYPOCO-KS33). (a) MSCL P-wave velocity; (b) MSCL porosity; (c) UHR P-wave velocity vertical profile the nearest to core locations (Table 2); (d) MERT resistivity vertical profile the nearest to core locations (Table 2); (e) Porosity calculated at the core locations from MERT resistivity using the Archie law detailed in the text.

Figure 7: MSCL P-wave velocity as a function of MSCL porosity for cores SYPOCO-KS32, SYPOCO-KS02 and SYPOCO-KS33. The solid black line is the result of a polynomial regression and is compared to published results. The grey dashed circle surrounds the values above the seismic mask zone.

Figure 8: Linear relationship between the logarithms of porosity and resistivity. The resistivity logarithm comes from MERT profiles at the core locations. The porosity logarithm comes from MSCL result, rescaled at the MERT depths. The core SYPOCO-KS02 is not presented for the modelling as its quality is inferior to cores SYPOCO-KS32 and SYPOCO-KS33.

Figure 9: Seismic UHR P-wave velocity as a function of porosity inferred from MERT models for areas C, D, E and F (Figure 2f). The solid black line is from the MSCL data in Figure 7. The dashed black line is a linear regression.